J. Condensed Matter Nucl. Sci. 17 (2015) 1–26

Research Article

Strained Layer Ferromagnetism in Transition Metals and its Impact Upon Low Energy Nuclear Reactions

Louis F. DeChiaro*
Naval Surface Warfare Center, 5493 Marple Road, Suite 156, Dahlgren, VA 22448, USA

Lawrence P. Forsley
Global Energy Corporation, Annandale, VA 22003, USA

Pamela Mosier-Boss
Space and Naval Warfare Systems Center (SPAWAR) Pacific, San Diego, CA 92152, USA

Abstract

Spin-polarized Density Functional Theory (DFT) calculations have been performed to model the lattice structures for the Transition Metal Group, Columns I and II, and a number of sp elements in the Periodic Table. Our results suggest that most of the transition metals can exhibit ferromagnetic ordering if the lattice is placed in sufficiently high tensile stress. These results are applied to the study of some layered structures employed by a number of Low Energy Nuclear Reaction (LENR) research teams and may help to explain some of the anomalous results and the difficulty in reproduction of those results.
© 2015 ISCMNS. All rights reserved. ISSN 2227-3123

Keywords: DFT, Epitaxial, Ferromagnetism, LENR

1. Introduction

Although much work remains to be done in the understanding and reduction to practice of Low Energy Nuclear Reactions (LENR), the body of experimental data accumulated over the past 25 years contains a wealth of clues to inspire and guide the LENR community. For example, since the early 1990s it has been known [1] that the amount of excess heat measured in a typical electrochemical LENR experiment can be increased by the appropriate application of a DC magnetic field. The Bockris Group at Texas A&M also reported [1] increased excess heat when their cells were stimulated with very high frequency (VHF) and ultra high frequency (UHF) electromagnetic fields. Finally, Letts and Hagelstein [2] reported excess heat when they focused the beams of two visible frequency lasers upon the cathodes

*E-mail: louis.dechiaro@navy.mil; Tel.: 1-540-653-8040.

© 2015 ISCMNS. All rights reserved. ISSN 2227-3123

in their Fleischmann–Pons cells, especially when the frequency difference between the two lasers corresponded to the THz atomic vibrational frequencies preferred by the PdH and PdD lattices. They also found that the best results were obtained when a DC magnetic field measuring about 700 Gauss was applied across the face of their Pd foil cathodes. As a result of these observations, a number of LENR community members believe that there are profound connections among LENR phenomena, atomic vibrations, and electromagnetic fields.

Experimental evidence also suggests that certain metal oxides may have a role in the LENR mechanism(s). For example, as we discuss in detail below, the layered structures used successfully by Iwamura et al. [3] contain thin films of CaO in addition to the expected Pd. And one of the well-known Arata structures [4] contains nanoparticles of Pd embedded in a nonconducting matrix of zirconium dioxide. However, the choice of oxide is apparently not arbitrary, because the Iwamura team also reported that using thin films of MgO instead of CaO yielded negative experimental results.

This paper presents the results of Density Functional Theory (DFT) computations performed to study itinerant ferromagnetism in elemental transition metals and strained layer superlattices of binary composition. Section 2 provides a short introduction to Density Functional Theory. Section 3 discusses the basic results, including the cross checks done to ensure credibility and physicality of the DFT output, extraction of values for the equilibrium lattice constant, and the lifting of the degeneracy between spin-up and spin-down electron energy eigenvalues. Section 4 presents our results on the ground state lattice energy and absolute magnetization versus lattice constant and introduces the concept of normalized asymptotic magnetization per unpaired valence electron spin. Section 5 discusses the experimental results reported by the Mitsubishi Heavy Industries (MHI) team led by Yasuhiro Iwamura and interprets them in light of the DFT spin-polarized results of this work. Section 6 presents the results of a DFT supercell study of the CaO:Pd interface and illustrates the degree of spin polarization of the various atomic species in the structure. Section 7 discusses the experimental results of Yoshiaki Arata in light of our DFT findings, and Section 8 contains the results of a DFT supercell study of the ZrO_2:Pd interface that may affect the Arata results in roughly the same way that the CaO:Pd interface affects the MHI results. Finally, Section 9 summarizes our results.

2. Density Functional Theory

Density Functional Theory (DFT) is a mathematical procedure that can be used to simulate small clusters of atoms and calculate from first principles (with essentially no adjustable parameters) many important physical properties such as ground state energy, lattice stress, electronic structure, phonon dispersion curves, and many more, given only the positions and atomic species for each atom in the cluster. Software implementing DFT makes use of the periodic symmetry of an ordered crystal lattice so that a finite-scope calculation based on a single unit cell of an ordered lattice can often produce results that approximate the bulk properties of a macroscopic sample of the material.

The algorithms used in such calculations originated in a mathematical proof in which Hohenberg and Kohn [5] presented a variational principle for obtaining the ground state energy of an electronic system, a principle that introduces a universal functional of the electron density $F[n(\vec{r})]$. Once this functional is computed by whatever means, the ground state energy in an arbitrary external potential can be obtained. The following year, Kohn and Sham [6] published a seminal paper in which they derived a highly nonlinear partial differential equation system that can be solved with a self-consistent, iterative algorithm to calculate the electron density versus position in an atomic system under study.

Several software packages implementing DFT are available. For this particular project, we chose Quantum Espresso, mainly because it has an excellent track record, it is available at no cost through the Web, and one of us (DeChiaro) had acquired several years' prior experience using Espresso in the academic domain. Further details, including the

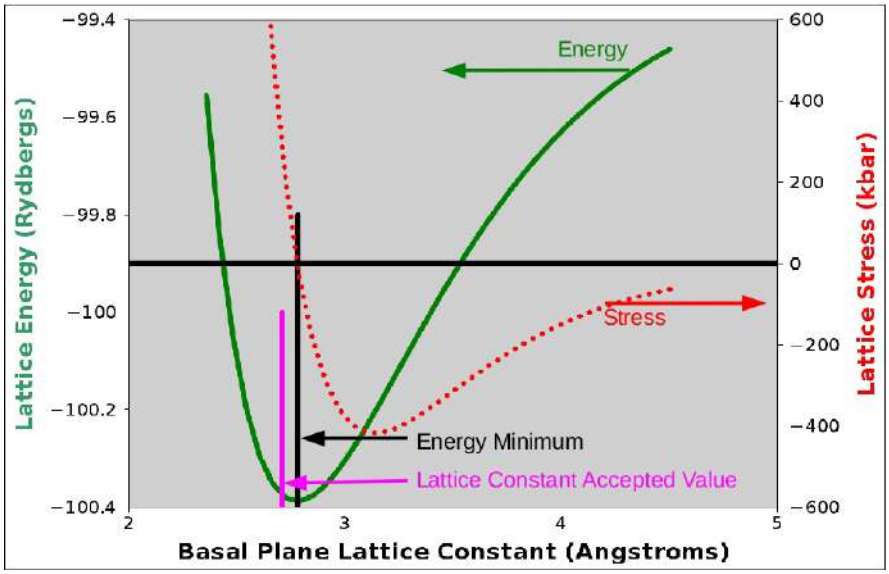

Figure 1. Lattice energy (left vertical axis) and stress (right vertical axis) curves vs. lattice constant for the paramagnetic solution of the transition metal ruthenium. Computed energy points are connected by solid green straight line segments, while the computed stress points are connected by dotted red straight line segments. The equilibrium lattice constant was found by fitting the three lowest energy points to a second order polynomial and then solving this to find the point of zero slope. The error between this value and the accepted value of lattice constant is about 2.7%.

algorithms used to solve the Kohn–Sham equation in a self-consistent iterative manner, are available in Giannozzi et al. [7], and the interested reader is directed to this publication.

Users of such software packages must be aware of a number of limitations and caveats. Each atomic species is represented by a pseudopotential file that approximates the effects of the atomic nucleus and the core electrons upon the valence electrons – but without the mathematically problematic "wiggles" and frequent zero crossings exhibited by the actual wave function. The generation of such pseudopotential files requires a parametrization procedure that vastly reduces the computational resources needed but also introduces certain errors. In general, we have obtained reasonably good results when using pseudopotential files parametrized with the Perdew, Becke, and Ernzerhof (PBE) generalized gradient approximation. However, in some cases, we employed Perdew-Zunger local density approximation pseudopotentials, generally because PBE pseudopotentials either might not be available for all elements or because the PZ potentials provide better agreement with experiment for some observable quantities. In any event, one should state which of the several different types of pseudopotential files were used, and these can be found in Appendix A for this work.

3. Basic Results: Extraction of the Lattice Constant

The ultimate success or failure of any computational model rests upon the degree to which it can accurately predict observable quantities such as the lattice constant. The DFT has had good success in accurately modeling many of the atoms in the Periodic Table, provided that one uses pseudopotential files that have been carefully tested and have good transferability characteristics. The two sections of the Table where the DFT success has been quite limited are the Lanthanide and the Actinide Series, primarily due to the difficulty in modeling the incomplete f-shells of those series.

Figure 1 shows the computed results for ruthenium, a typical example of a well-behaved species near the center of the Transition Metal Group. The reader will note that the extracted value of lattice constant corresponding to the energy minimum is in excellent agreement with the zero crossing of the lattice stress curve. This is a necessary but not sufficient condition to ensure that the calculated results are physically meaningful. One of the other important conditions that must be satisfied is a reasonable agreement (less than 5% error) between the extracted value of equilibrium lattice constant and the accepted value. Some of the elements crystallize in multiple lattice types and/or are characterized by multiple c/a ratios in the literature, however in all cases it was possible to find a structure that was stable and yielded good agreement between computed and accepted values of lattice constant. For most of the elements, we employed values from Wyckoff for the accepted lattice constants. Appendix A contains a table that compares the computed and accepted values of lattice constant for all the atomic species in this study. The mean absolute value of all these errors is about 1.565%, confirming the published results that DFT is reasonably successful in modeling the behavior of most of the atomic species of the Periodic Table in their elemental lattice form.

One further caveat that should be borne in mind when interpreting these results has to do with the crystal structures. We employed the lattice types, space groups, and atomic coordinates as specified in Wyckoff for one of the structures

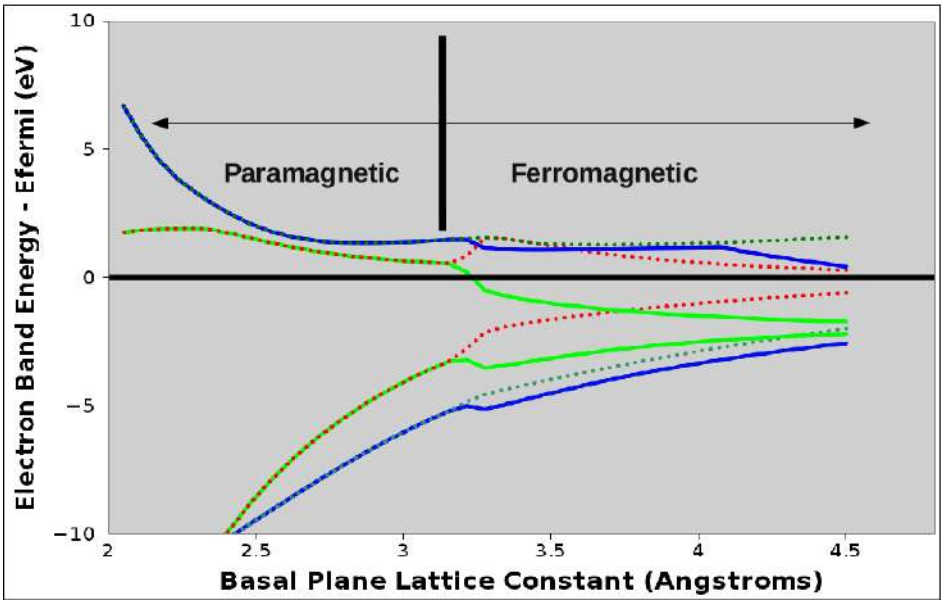

Figure 2. Electron energy relative to the Fermi level vs. lattice constant for the ferromagnetic solution of the transition metal ruthenium. Computed points on the spin-up bands are connected by solid straight line segments, while the points on the spin-down bands are connected by dotted straight line segments. The light green and red curves illustrate the two bands lying closest to the Fermi level, while the dark green and blue curves illustrate the two bands lying furthest from the Fermi level.

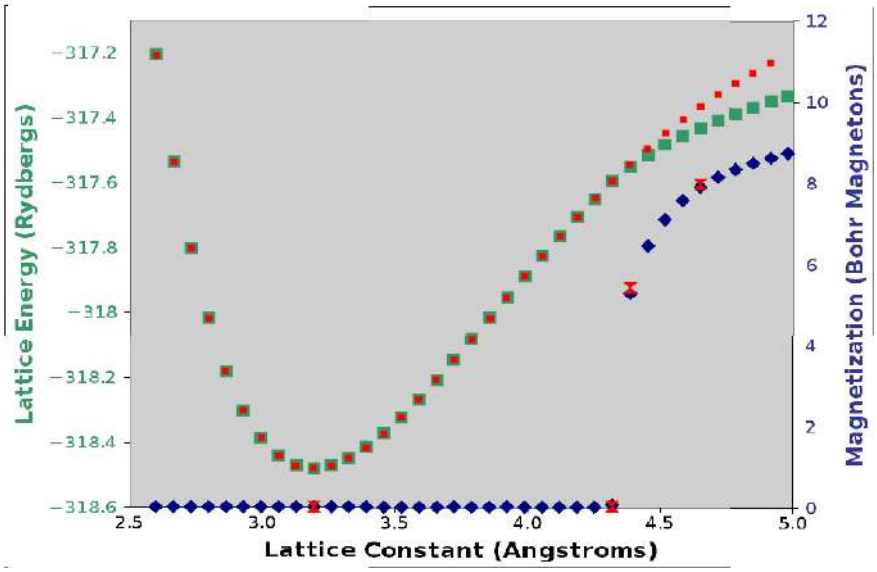

Figure 3. Ground state lattice energy (left vertical axis) in Rydbergs and absolute magnetization (right vertical axis) for tungsten versus BCC lattice constant in Angstroms. The green squares show the ground state energy for the ferromagnetic solution, while the small red squares show the energy for the paramagnetic solution. The blue diamonds show absolute magnetization in Bohr Magnetons per unit cell, and the red hour-glass symbols show magnetization values at key points calculated with a very dense mesh of k points to ensure maximum accuracy.

that is in equilibrium at room temperature. The abscissas of the plots presented in this work include values of lattice constant corresponding to high tensile stress. Such stress represents a departure from equilibrium conditions that will significantly elevate the lattice energy. All materials are limited in the associated strain they can support without physical destruction of the lattice. Atomic systems also possess a number of mechanisms to reduce their energy, even when the strain lies below the threshold for catastrophic destruction. These include the nucleation of lattice defects such as dislocations, the possibility of a phase transition to a different lattice type and space group, and even the growth of whiskers (for which high purity silver and tin are both notorious). Some of these phase transitions are accompanied by physical displacement of the atoms, for example, when a face-centered cubic (FCC) lattice undergoes a tetragonal distortion as the result of an applied stress field. Other phase transitions, however, do not displace the atoms but instead cause a change in electronic structure that gives rise to a collective phenomenon known as itinerant ferromagnetism. Materials that exhibit this latter type of phase transition are characterized by a critical threshold value of lattice constant at which the numerical solution to the Kohn–Sham equation suddenly bifurcates into two distinct solutions. One of these is paramagnetic and joins continuously and smoothly with the paramagnetic behavior found below the threshold. However, the other solution is ferromagnetic in nature and may exhibit discontinuities in the derivatives of certain parameters as it joins with the paramagnetic solution at the threshold value of lattice constant. One of those parameters is the electronic band structure, which bifurcates at the threshold into two distinct sets of energy bands, one for the spin-up electrons, the other for the spin-down electrons. This bifurcation usually does not affect the deep core states, but will significantly perturb the energy bands lying near the Fermi surface. To illustrate an example of this behavior, we return to the case of ruthenium.

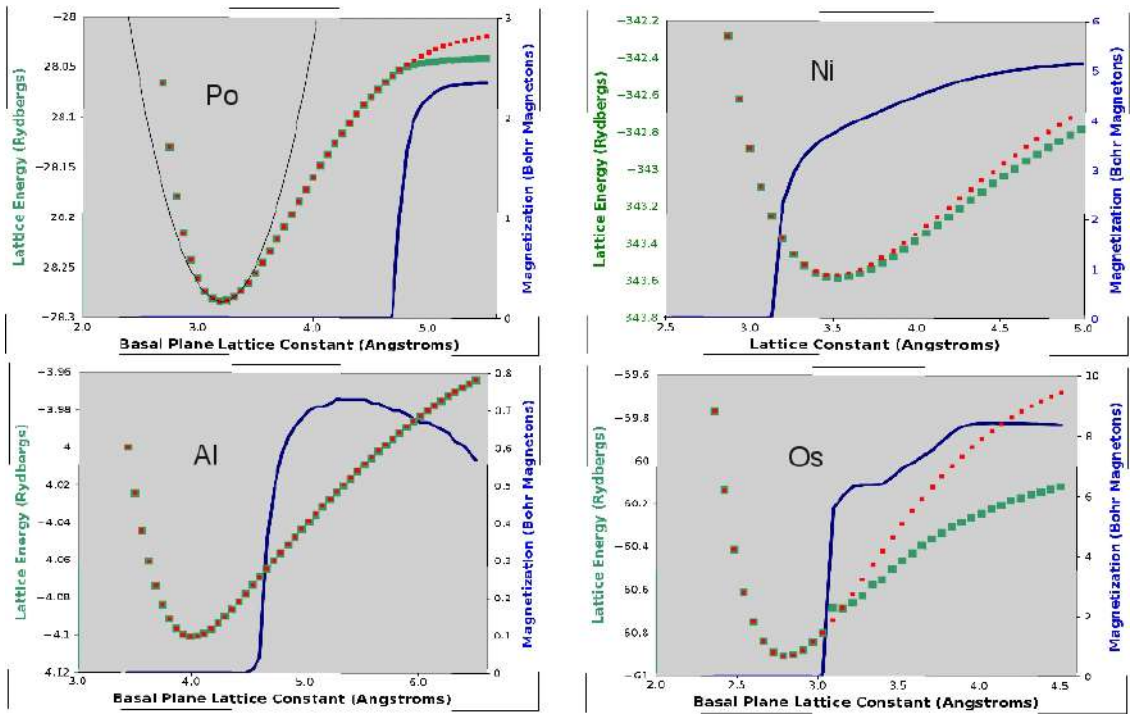

Figure 4. Ground state lattice energy (left vertical axes) in Rydbergs and absolute magnetization (right vertical axes) for polonium (upper left), nickel (upper right), aluminum (lower left), and osmium (lower right) versus lattice constant in Angstroms. Once again, the green squares show the ground state energies for the ferromagnetic solutions, while the small red squares show the energies for the paramagnetic solutions. The dark blue curves show absolute magnetizations in Bohr Magnetons per unit cell, and the thin black parabolic line on the polonium plot shows the regression polynomial that was fitted to the several points near the energy minimum and used to extract a value for the equilibrium lattice constant.

Figure 2 shows the electron energy eigenvalues (relative to the Fermi energy) plotted as a function of lattice constant for four spin-up and four spin-down energy bands at the center of the Brillouin zone ($k = 0$) where the electron momentum vanishes. Two of these energy bands lie below the Fermi surface, while the other two lie above it. The two bands lying closest to the Fermi surface are shown plotted in brighter colors, while the two lying furthest are plotted in darker colors. It is evident that the two brighter colored plots showing the bands lying closest to the Fermi surface exhibit considerably more splitting than the bands lying further from the surface.

4. Lattice Ground State Energy and Absolute Magnetization

The two most important lattice parameters to be considered in this work are the ground state energy and the magnetization of the lattice. The overall lattice ground state energy is the primary quantity used by Quantum Espresso in governing the self-consistent field (SCF) iterative solution of the Kohn–Sham equation. This ground state energy is normally given in units of Rydbergs (the energy level for the solitary 1s electron in hydrogen is -1.0 Rydberg or -13.6 eV), and the SCF iteration normally proceeds until the estimated iterative increment in this quantity falls below a user-specified threshold that is typically 10^{-8} Rydberg. Magnetization is calculated as the spin-up minus the spin-down charge density versus position in the three dimensional working volume of the structure specified by the user in the input file. These two spin-polarized charge densities are normally identically equal in materials that have no absolute magnetization

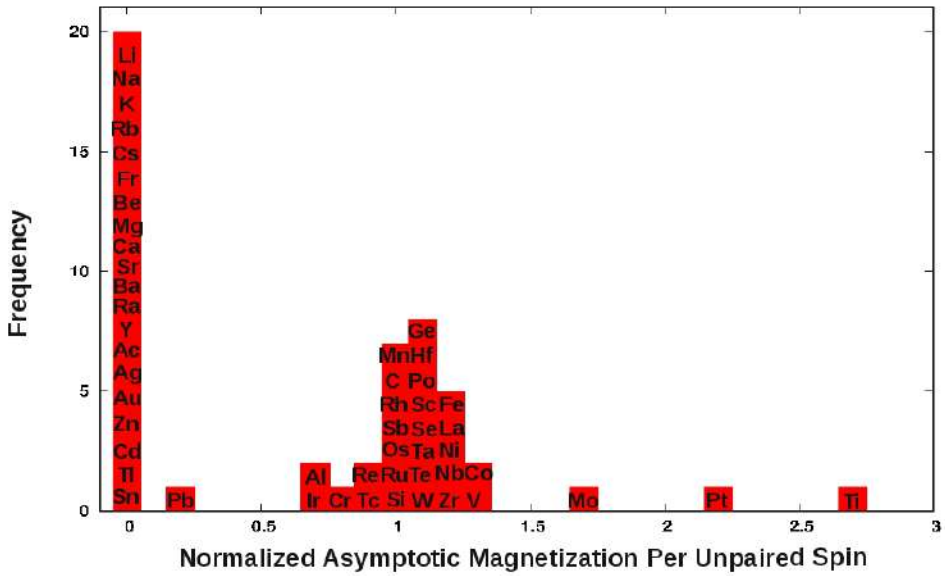

Figure 5. Histogram plot showing the distribution of the computed asymptotic magnetization for the elements after normalization to yield the absolute magnetization per unpaired electron spin. The width of each numerical bin is 0.1, and each vertical bar contains the chemical symbols of the various elements whose normalized asymptotic magnetizations fall in its respective bin. The tall bar at 0 on the left shows the 20 elements whose outermost electron shells contain only s electrons; they do not develop ferromagnetic activity when placed under high tensile stress.

and where the spin-up and spin-down electron energies are everywhere equal. However, as can be seen in Fig. 2, one of the spin-up energy bands crosses the Fermi surface at a lattice constant value near 3.2Å, while the corresponding spin-down band remains above the surface.

Since the electron occupation numbers (as specified by the Fermi–Dirac distribution) rapidly drop toward zero as one crosses the Fermi Surface from below, the spin-up band will be filled at $k = 0$ while the spin-down band will not be filled. Thus, we expect that the system will begin to show a nonvanishing magnetization, and the ground state lattice energies for the paramagnetic and the ferromagnetic solutions may begin to diverge from one another. This behavior is illustrated in Fig. 3, where we present ground state energies for the paramagnetic and ferromagnetic solutions and absolute magnetization (proportional to $\int \mid \rho_{\text{up}} - \rho_{\text{down}} \mid \mathrm{d}^3 V$) versus lattice constant for the transition metal tungsten.

Initial conditions specified in the input files were chosen to encourage the system to converge to either the paramagnetic or the ferromagnetic solution. For all points to the left of the threshold value of about 4.32Å, the ferromagnetic solution does not exist, and the code always converged to the paramagnetic solution, regardless of initial conditions. However, for points above threshold, the two solutions coexist, and the choice of initial conditions determines which solution will "attract" the convergence of the algorithm. The reader will note that at the threshold, we see the energy curves for the two solutions begin to diverge. The difference between the two grows monotonically with increasing lattice constant for tungsten in the range of lattice constants explored in this work. Not all atomic species exhibited this monotonic increase. However in nearly all cases, the ferromagnetic energy was lower than the paramagnetic energy at the same lattice constant, suggesting that the ferromagnetic state is the energetically preferred one. The very few exceptions involve one or two points close to the thresholds where the numerical fluctuations are very large for some elements. This can cause difficulty in convergence and the possibility of critical fluctuation noise in the results, a situation very common in the study of thermodynamic phase transitions. Figure 4 shows results for four other elements, drawn

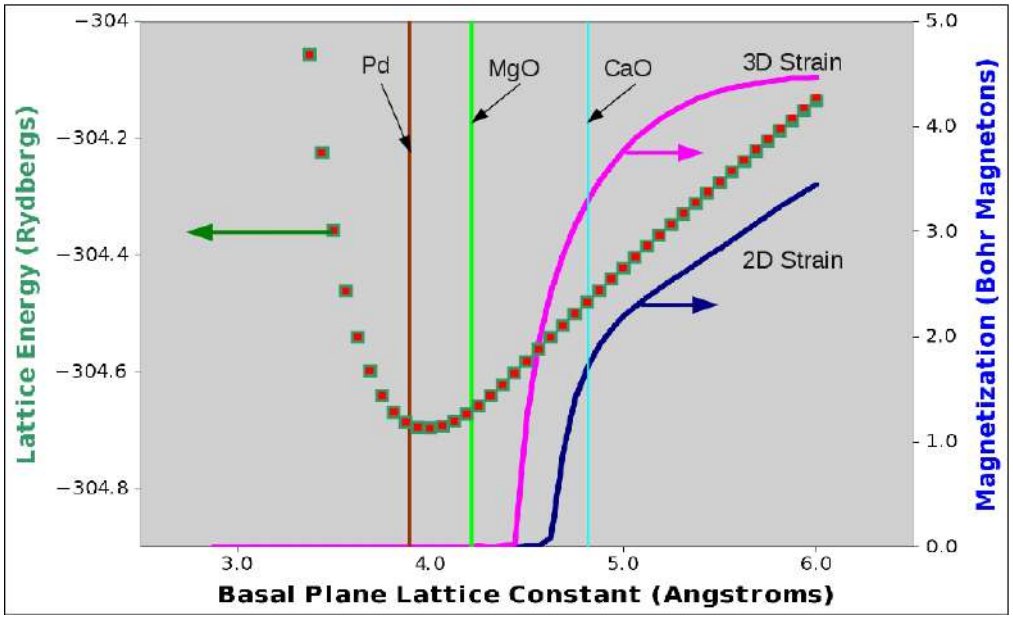

Figure 6. Simultaneous plots showing the ferromagnetic (green squares) and paramagnetic (small red squares) energy curve for Pd on the left vertical axis, the magnetization of Pd on the right vertical axis when strained in two and three dimensions, and the equilibrium lattice constants for Pd, MgO and CaO – all versus lattice constant.

from both the transition metals (Ni and Os) and the so-called sp elements (Al and Po) where the outermost valence electrons in the isolated atoms lie in p orbitals. We see that the general trend shows a rapid increase in magnetization at the threshold, a saturation at higher lattice constants, and in some cases, a decrease in magnetization at very high lattice constants as seen in the Al curves. The one element from the figure that is known to be ferromagnetic under normal conditions is nickel, and it is no coincidence that the threshold for bifurcation of the energy surface lies below the equilibrium lattice constant. Finally, we note that the 4 elements shown in the figure exhibit considerable differences in the rates at which the paramagnetic and ferromagnetic energy surfaces diverge above threshold. The ratio between this energy difference and kT is likely to have a strong influence upon the rate at which the higher-energy paramagnetic state is thermally populated at any given absolute temperature above 0K.

In the limit as the lattice constant approaches infinity, the behavior of the system approaches that of isolated atoms, for which the intrinsic electronic magnetic moment (neglecting the contribution caused by the orbital motion of the electrons) will be equal to the number of unpaired electron spins multiplied by the Bohr Magneton. In this limit, we would expect the total moment for a system of N decoupled identical atoms to be equal to the product of N, the number of unpaired spins in each atom, and the Bohr magneton. This implies that if we take the total moment of the system and normalize it by dividing by this quantity, we should obtain 1.0 Bohr magnetons per unpaired spin. The magnetization plots shown in Fig. 4 encompass about one order of magnitude dynamic range for the peak magnetizations computed in this work. Approximately the same can be said for the variation across the Periodic Table in the product of N and the number of unpaired spins. If we suspect these two quantities to be correlated in real elemental lattices, then we should be able to extract or extrapolate the maximum magnetic moment from each of the plots, perform the normalization, and obtain a result close to 1.0 in the absence of competing effects. This exercise was performed for each of the atomic species in this study. However, before presenting the results, we should add that it would be surprising if the

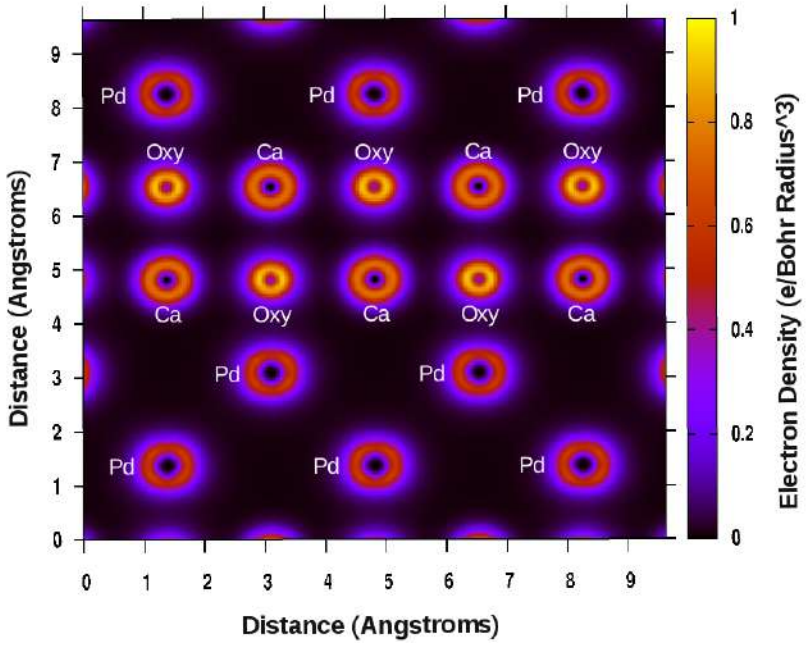

Figure 7. False color cross-sectional image of total charge density taken parallel to the *YZ* plane (thus along the [100] crystal plane) and intersecting the CaO:Pd supercell. Individual atoms are labeled for clarity. This image should be used to locate the various atoms and simplify the interpretation of the more complex spin-polarized image shown in Fig. 8.

magnetic moment contributions resulting from the electron orbital angular momenta were found to have no impact upon the results. In fact, our calculations indicate that in one respect the orbital angular momentum quantum number does impact the magnetizations of the elemental metals and semi-metals. Within the limits of computational precision caused by the numerical fluctuations, the magnetizations of all Column I and Column II atoms (whose outermost electron shells are comprised entirely of s-state electrons with vanishing orbital angular momenta) are exactly zero. The same can be said for the atoms lying along the extreme right hand edge of the Transition Metal Group (Zn, Cd, and Hg). We studied the first two of these and obtained zero magnetization and no ferromagnetic solutions to the Kohn-Sham Equation for any lattice constant lying in the range of values studied herein. Most of the remaining transition metals we studied (with the sole exceptions of Y, Ac, Ag, and Au) and some of the sp elements exhibited nonzero values of magnetization for sufficiently large values of lattice constant. Figure 5 contains a plot of the probability density function censored to the form of a histogram for the distribution of normalized peak magnetizations per unpaired spin.

With the exceptions of the elements whose outermost electron shell contains only s electrons, most of the elements produced normalized asymptotic magnetizations that cluster fairly close to the expected value of 1.0. The element Pd could not be plotted on Fig. 5 because the outermost shell is the 4d shell, and it is completely filled in the ground state. Thus there are no unpaired spins at all, unless the lattice can be sufficiently excited to cause some of the atoms to occupy the low-lying first excited state corresponding to an electronic configuration of 4d9 5s1. If this were the case, then Pd would appear in the distribution at 1.125 in the tallest of the histogram bars clustered near 1.0.

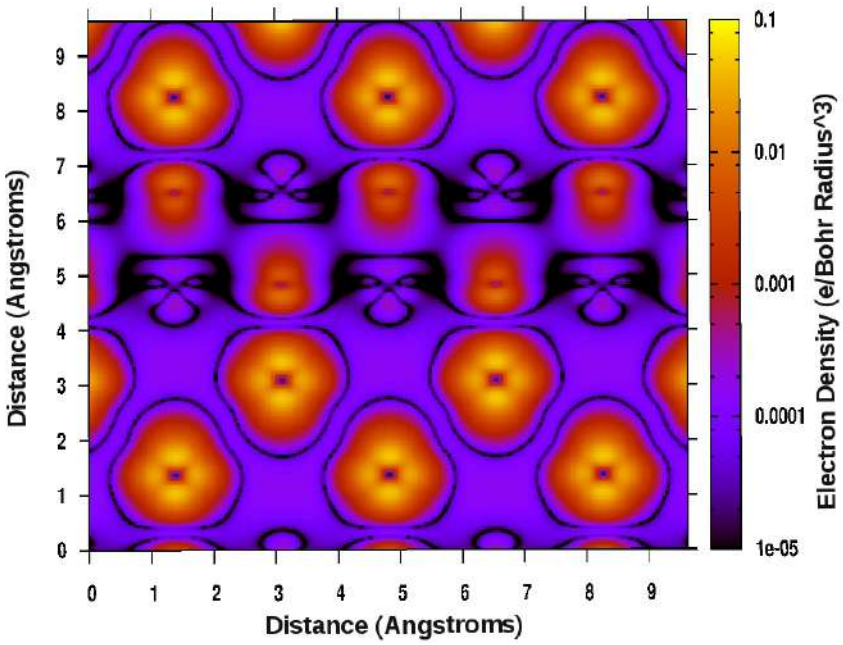

Figure 8. False color cross-sectional image of absolute value of spin-up minus spin-down charge density taken parallel to the *YZ* plane (along the [100] crystal plane) and intersecting the CaO:Pd supercell. A logarithmic scale was used to grade the colors in order to show all the atoms, including the most inactive ones. Atoms that are highly spin polarized will be bright in this image, while totally inactive atoms will appear black.

5. Application to the Iwamura Structure

From 1996 to 2005 results from a series of key LENR experiments were published by a team of workers at Mitsubishi Heavy Industries under the direction of Yasuhiro Iwamura. These results include the reported observation of excess heat and several types of nuclear transmutations that change the atomic number of their reactant species by +4 and the atomic mass number by +8 when deuterium is forced under a pressure difference of about 1.7 atm. through an ABABAB sandwich structure consisting of alternating layers of Pd and a light metal oxide having the same FCC crystal structure as Pd. Some of the Iwamura results were recently confirmed by an independent team at Toyota Central Research Laboratories [9] and published in the October, 2013 Issue of *Japanese J. Appl. Phys.* Iwamura et al. also presented some of their key findings at ICCF-11 in Marseilles, France, in 2004. Among these findings are the following observations:

(1) Transmutations are not observed when the light metal oxide layers are absent from the sandwich structure.
(2) Transmutations are not observed unless the sandwich structure is permeated with D_2 under pressure.
(3) Transmutations are not observed if the light isotope of hydrogen is used instead of deuterium.
(4) Transmutations are only observed for some chemical compositions of the light metal oxide layers and not others. In particular, when Pd is used as the transition metal layer, CaO was observed to function well, while MgO (another oxide with the same crystal structure) did not function at all.

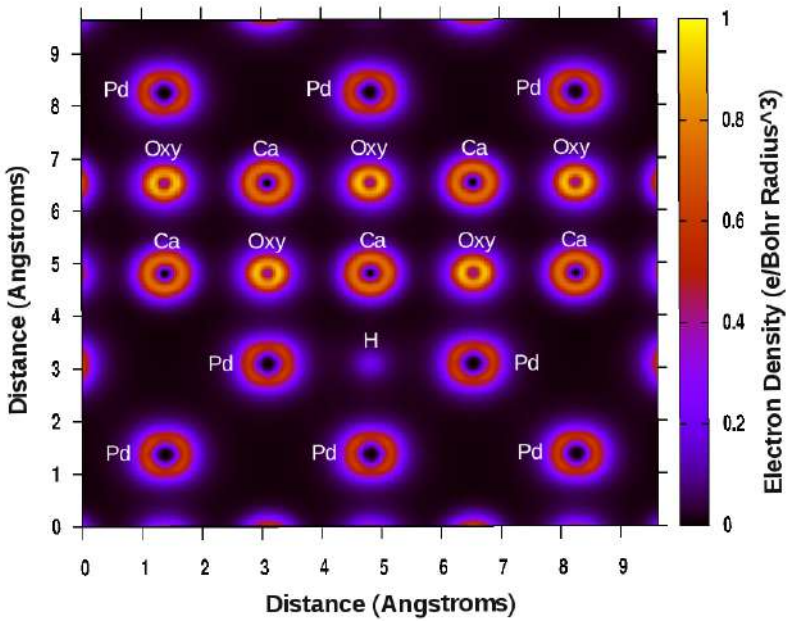

Figure 9. False color image of total charge density (in units of electronic charge per cubic Bohr radius) versus position after a single hydrogen atom has been added at the octahedral site just below the calcium atom near the geometric center of the image. The hydrogen atom can be seen as a small, purple sphere.

The Mitsubishi team suggested that two possible roles of the oxide layers are to increase the deuterium density within the structure and to modify the surface electronic band structure of the Pd in some way that would favor the LENR reactions. Based upon the results of our spin-polarized DFT studies, it is now possible to propose a third role for the oxide layers: to apply a tensile stress to the Pd films in two dimensions that is of sufficient magnitude to drive at least some fraction of the Pd atoms into their ferromagnetic state. If this third hypothesis is experimentally confirmed, we would then interpret the sandwich structure as a long period strained layer superlattice that is very similar (except for its longer period) to those now widely employed by the integrated circuit and optoelectronic component industries to create new materials with novel and highly optimized properties.

Figure 6 presents results that help explain how the strained layer superlattice hypothesis functions. The accepted value for the Pd lattice constant is shown as a brown vertical line in the figure. As we might hope, this value lies very close to the global minimum in the energy curves. The lattice constant for MgO as shown by the light green line in the figure is larger than that of Pd, but not sufficiently large to drive the Pd into its ferromagnetic state when the sandwich structure is epitaxially grown so that some fraction of the Pd is forced to take on the lattice constant of the underlying MgO. Thus, *if* the LENR reaction were to depend upon the presence of a large magnetic field, we would predict that the sandwich structures made from MgO will not perform any better than those without any metal oxide layers at all – in agreement with the experimental observations. On the other hand, the lattice constant of CaO (4.815 Å) is considerably larger than that of MgO, as one can see in the light blue vertical line in the figure. In fact, the lattice constant of CaO is sufficiently large that if we get some epitaxial growth of the Pd on top of the CaO so that the Pd is forced to assume the CaO lattice constant, we expect the Pd to be driven well into its ferromagnetic state, regardless of whether the tensile stress is applied in 3 or only 2 physical dimensions. This is also in excellent agreement with experiment.

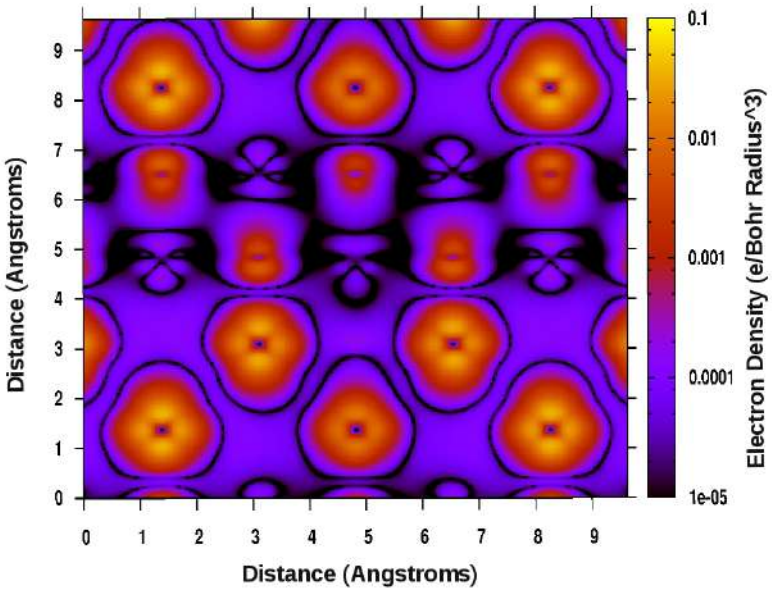

Figure 10. False color cross-sectional image of absolute value of spin-up minus spin-down charge density after adding the single hydrogen atom. The hydrogen is barely visible just below the central Ca atom and above the center-most Pd atom. Please note that the "eyes" of the central Ca atom are now missing, and the brightness of the Pd atom immediately below the hydrogen and the oxygen directly above the hydrogen is smaller than the other Pd and oxygen atoms, respectively.

As with any hypothesis, further experiments would be necessary either to confirm or refute it. However, if confirmation is obtained, the insight gained could illuminate the path toward technological exploitation. Among other things, it could provide guidance for those seeking other metal insulating compounds with even larger lattice constants (such as BaF_2, for example, with a lattice constant near 6.2 Å). There is, of course, a maximum percentage lattice constant mismatch between the two materials (typically only a few percent) that can be tolerated without negative effects such as delamination of the epitaxial film, nucleation of dislocations or other crystallographic defects, and thermal expansion problems, to name just a few. Thus the quest for the optimum set of materials for any given application will be far from trivial.

6. DFT Studies of the CaO:Pd and MgO:Pd Interfaces

The lattice structures for most of the elemental metals contain a basis with only one or at most two atoms. This makes it possible to study such structures even when limited to a single core processor. However, the study of an interface between two materials usually requires construction of a much larger system containing at least several tens of atoms. Fortunately, the authors have access to a desktop Linux machine with 16 cores and 16 GB of RAM, establishing an upper limit on the accessible systems at about 75 atoms. We therefore modeled the CaO:Pd interface by constructing a supercell of $2 \times 2 \times 2$ FCC unit cells, the bottom 4 of which are composed of Pd and the top 4 of CaO. The overall lattice constant for the supercell was set at twice the value for a single cell of CaO. This should be reasonably accurate in the limit as the CaO layer becomes much thicker than the Pd layer. Quantum Espresso saves both the many electron wave function and the spin-polarized charge density as arrays defined on a discretized three dimensional mesh. The post-processing tool makes it straightforward to sample the wave function and charge density on any user-specified line

Figure 11. False color cross-sectional image of total charge taken parallel to the *YZ* plane (along the [100] crystal plane)and intersecting the MgO:Pd supercell. Individual atoms are labelled for clarity. The Mg atoms are not visible because they are represented in the pseudopotential file only by their two valence electrons, which have been completely absorbed into the electronic band structure of the material and are no longer localized around the ion core. The Mg labels show where the ion cores lie.

or plane intersecting the volume of the system under study. When combined with a full featured plotting program such as Gnuplot, the user can generate false color images showing total charge density versus position, spin up minus spin down charge density versus position, and many other useful parameters.

Figure 7 shows a false color cross-sectional image showing total charge density through the *YZ* ([100]) plane of the supercell. Individual atoms are labeled to facilitate their species identification. The atoms appear as doughnut-shaped objects because the pseudopotential files used to represent each atom contain only the outermost valence electrons, the ones most directly involved in the creation of chemical bonds and the determination of most physical properties of materials. Figure 8 shows a false color cross-sectional image through exactly the same set of atoms, however here we are plotting the absolute value of spin-up minus spin-down charge density as a function of position with a logarithmic color scale in order to assess which atoms are the most ferromagnetically active. The largest and brightest atoms in Fig. 8 are Pd, and the spin polarized image shows evidence of the four-fold symmetry of the FCC lattice. We thus appreciate that the Pd has indeed become spin polarized by virtue of the tensile stress applied by the CaO lattice with which the Pd is in contact.

The thin black regions surrounding each Pd atom represent places where the spin polarization goes through a zero and switches algebraic sign. Since the straight line path from one Pd to another passes through exactly two of these sign changes, we see that all the Pd are ordered ferromagnetically with respect to one another. The smaller of the bright atoms are the oxygens, and we note that these are also spin polarized and ferromagnetically ordered relative to the Pd

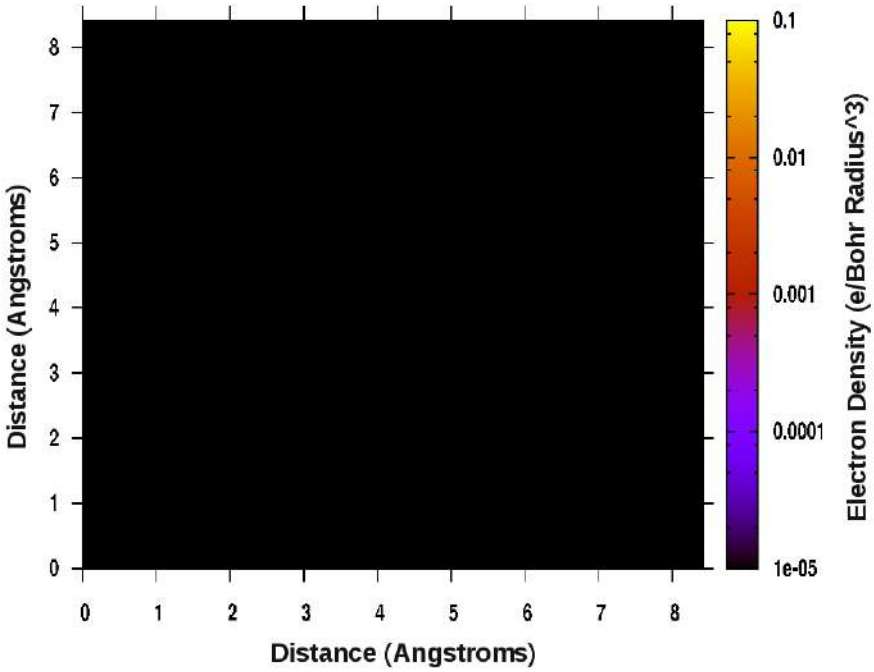

Figure 12. False color cross-sectional image of absolute value of spin-up minus spin-down charge density taken parallel to the *YZ* plane (along the [100] crystal plane) and intersecting the MgO:Pd supercell. The same logarithmic scale as presented in Figs. 8 and 10 was used to grade the colors. The entire image is black, confirming our prediction that the structure does not show any ferromagnetic ordering.

atoms. We also note that all the Pd atoms are equally magnetized. The shape of the spin polarized regions of the oxygen atoms is somewhat reminiscent of "Fig. 8" shape of the p orbitals that serve as the outermost occupied orbitals for the oxygen atoms. Finally, the least magnetically active of the three atomic species in Fig. 8 is the sublattice of calcium atoms. These atoms can easily be distinguished from the other species by their faint resemblance to the face of a masked and bearded burglar. The very low level of magnetic activity for the Ca atoms is consistent with our monatomic results for calcium showing zero spin polarization for all of Columns I and II elements.

In order for the CaO:Pd layered structure to be technologically useful for performing transmutations, one must permeate the structure with deuterium under a modest pressure differential. It is therefore of interest to seek some insight into how the structure will change when the octahedral sites on the Pd layers are occupied by hydrogen atoms. The minimum perturbation possible involves the addition of just one hydrogen atom, and the most aesthetically-appealing place to add this atom is immediately above the center-most Pd atom. Figure 9 shows the total electron density false color image of the CaO:Pd structure with the single added hydrogen, and Fig. 10 shows the corresponding spin-polarized image.

Figures 7–10 are in good agreement with the prediction that the CaO:Pd structure can be expected to show itinerant ferromagnetic ordering. Equally important, however, is the exploration of the MgO:Pd structure. If the results of Fig. 6 are in fact correct, then we expect that a DFT study of the MgO:Pd structure with the supercell lattice constant set to twice the equilibrium value for MgO (4.211 Å) should result in no observable ferromagnetic ordering. Figures 11 and 12 show the results of the MgO:Pd calculation. Figure 11 shows a false color image of the total electron density vs. position in the *YZ* ([100]) plane at $x = 0$, and Fig. 12 shows an image of the spin-up minus spin-down charge

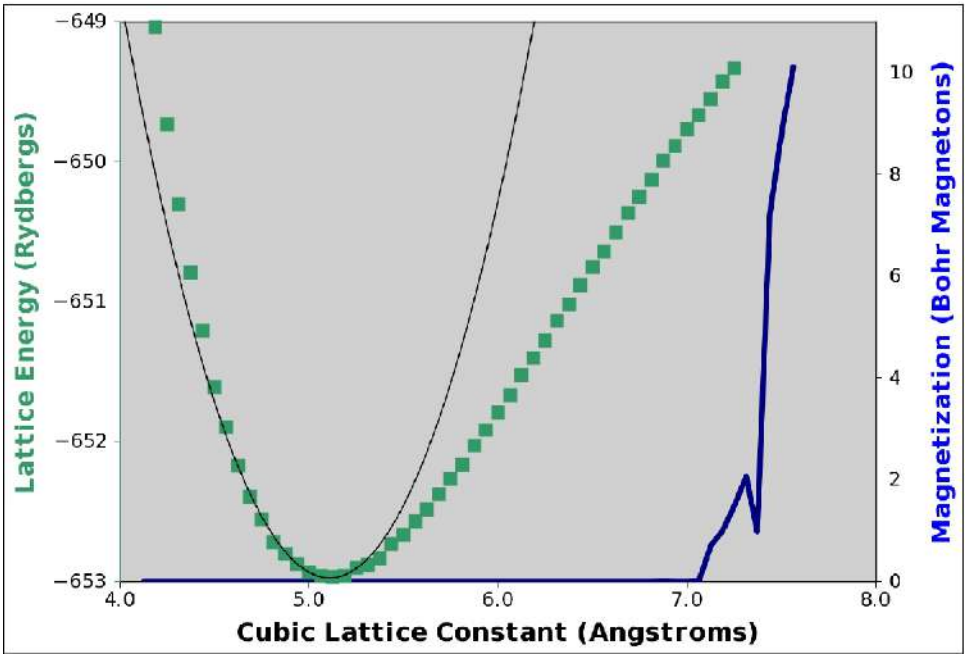

Figure 13. Ground state lattice energy (left vertical axis) in Rydbergs and absolute magnetization (right vertical axis) for cubic zirconia (ZrO_2) versus FCC lattice constant in Angstroms. The green squares show the ground state energy for the ferromagnetic solution, and the blue line shows absolute magnetization in Bohr Magnetons per unit cell. The narrow black line is the regression parabola that was derived by fitting the five points at the bottom of the energy curve to a second order polynomial. The extracted value of lattice constant is 5.1082 Å versus an accepted value of 5.07 Å.

density for the structure. The scales used in Figs. 11 and 12 are identical to those in Figs. 7 and 8, respectively. Aside from the "missing" valence electrons removed from the Mg atoms, the image shown in Fig. 11 closely resembles that of Fig. 7. In fact, the most obvious difference between the two figures is that the atoms appear slightly larger in Fig. 11. This is entirely due to the fact that the lattice constant in the MgO:Pd structure is considerably smaller (2×4.211 versus 2×4.815Å) than the lattice constant in the CaO:Pd structure, as is evident from the X and Y axis scales.

Finally, we note that the image in Fig. 12 is entirely black because there is no spin polarization down to the level of 10^{-5} electrons per cubic Bohr radius in the MgO:Pd structure, thus confirming our expectations that no spontaneous magnetization will appear because the Pd has not been strained up to its threshold for spontaneous ferromagnetic ordering. One dimensional cross sections were also performed for the same supercell runs (CaO:Pd with and without the single added H atom and MgO:Pd) whose two dimensional spin polarization false color images are shown in Figs. 8, 10, and 12. In order to avoid undue increases in the length of the paper, their plots are presented in a Supplemental Section contained on-line.

7. Application to the Arata Structure

Yoshiaki Arata of Osaka University has published a number of interesting papers in which he and his colleagues report several experimental observations that may be relevant to the computational results presented in this work. ZrO_2:Pd structures were fabricated by alloying Pd and Zr and subsequently oxidizing the alloy. Since Zr has a much higher chemical affinity for oxygen than Pd does, we end up with Pd nanoparticles embedded in an insulating matrix of ZrO_2

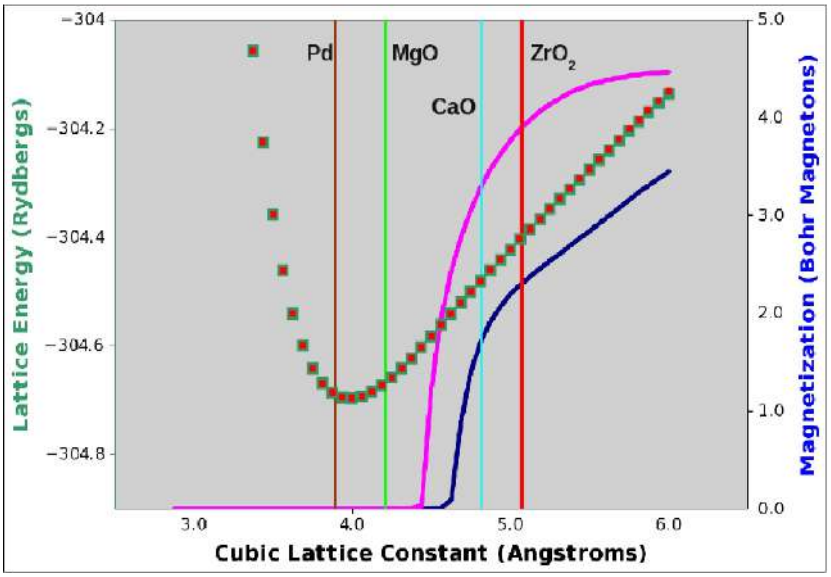

Figure 14. Simultaneous plots showing the ferromagnetic (green squares) and paramagnetic (small red squares) energy curve for Pd on the left vertical axis, the magnetization of Pd on the right vertical axis when strained in two and three dimensions, and the equilibrium lattice constants for Pd (brown), MgO (light green), CaO (light blue), and ZrO_2 (red) – all versus lattice constant.

(which can crystallize as the well-known cubic zirconia). The main experimental observations can be summarized as follows:

(1) Stimulation of the ZrO_2:Pd powder with ultrasonic power greatly increased the LENR rate.
(2) Stimulation of the ZrO_2:Pd powder with energy from a welding laser [10] greatly increased the LENR rate. In his ICCF-10 paper, Arata et al. do not state what kind of welding laser they employed. However, a literature search of Arata's other papers [11] strongly suggests that the laser was likely to have been a CO_2 laser. In fact, Arata invented the CO_2 laser welding process.
(3) LENR events, including the generation of significant quantities of ^{4}He, were observed when the ZrO_2:Pd powder was loaded with deuterium. No ^{4}He was observed when the pure light isotope of hydrogen was used.
(4) No ^{4}He was observed when the experiment was run with bulk Pd.
(5) The use of Pd black powder resulted in a low level of ^{4}He. The use of Pd nanoparticles resulted in higher ^{4}He levels, but not nearly as much as when the ZrO_2:Pd powder was used.

In light of the computational results presented in the previous sections of this work, we performed DFT studies of the cubic zirconia lattice with results presented in Fig. 13.

The error between the extracted value of lattice constant and the accepted value is about 0.75%, thus the most basic of the DFT results are in reasonable agreement with observation. The reader will note our DFT results predict that ZrO_2 can become ferromagnetic if it is placed in sufficiently high tensile stress. However, we do not expect this to happen in the Arata structure, because the ZrO_2 is placed in contact with Pd, which has a smaller lattice constant, thereby placing the zirconia in compressive stress. Having verified the lattice constant for FCC cubic zirconia, we next inquire how this value compares with the threshold for the onset of spontaneous ferromagnetic ordering in Pd. Results are shown in Fig. 14.

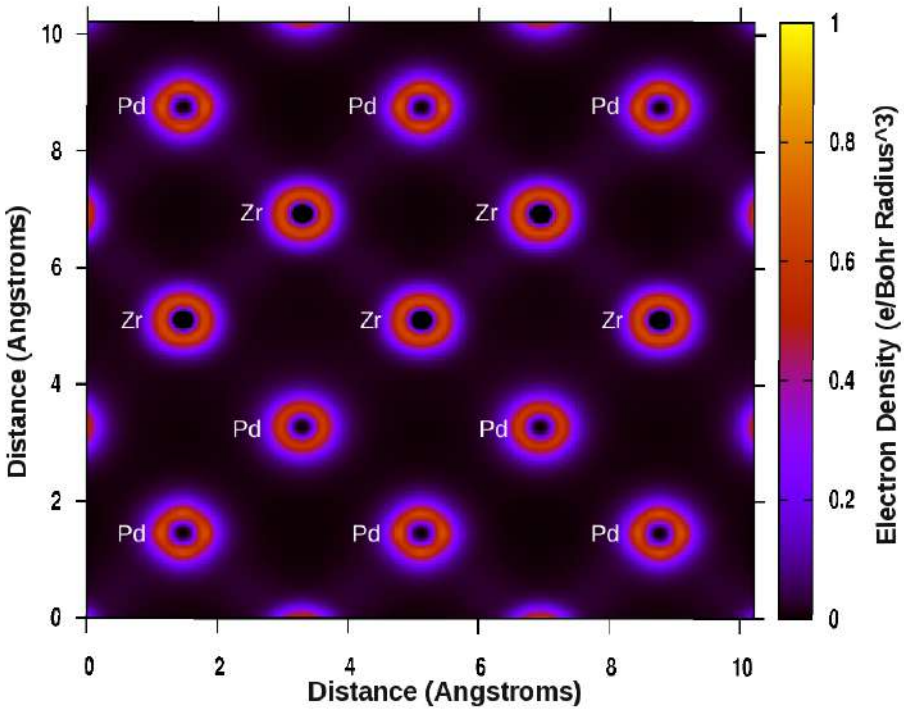

Figure 15. False color cross-sectional image of total charge taken parallel to the *YZ* plane (along the [100] crystal plane) and intersecting the ZrO_2:Pd supercell. Individual atoms are labeled for clarity. However, the oxygen atoms are not visible in this view because they occupy lattice sites located above and below the plane being represented in the figure. The Pd atoms can be distinguished from the Zr because the Pd core hole is smaller due to the higher nuclear charge. In addition, the Pd 4d valence charge cloud exhibits a slightly higher contrast around the circumference than the Zr atoms.

As we can see from the figure, cubic zirconia has a lattice constant larger than any of the substrates used by the MHI team. This suggests that growing Pd on a zirconia substrate will push the fraction of Pd cells that grow epitaxially further into the ferromagnetic regime than using MgO or even CaO. Indeed, the figure suggests that if the LENR rate is somehow driven by the local magnetic field intensity, we may expect to see rates for the Arata structures that are higher than those reported by the MHI team with their CaO substrates, provided only that the larger lattice constant of ZrO_2 does not cause the fraction of Pd cells growing epitaxially to plummet.

Before leaving the subject of the Arata results, we should comment on the use of the CO_2 laser and draw a connection with the work of Letts and Hagelstein. It is by now well-known that the output wavelength of a CO_2 laser is about 10.7 μm. When this free space wavelength is converted to frequency, we get a value of about 28.04 THz, which does not agree very well with the A1g stretching mode frequencies of 88.9, 108.8, and 125.7 THz for the D_2, HD, and H_2 free-space molecules, respectively. However, once the molecules are added to a monovacancy within the Pd lattice and the structure is relaxed to allow the hydrogen/deuterium atoms to find locally minimum energy positions, we calculate a number of phonon energy eigenvalues that lie in the 20–35 THz frequency range, depending upon which of several minimum energy sites are occupied by the hydrogen/deuterium molecules. Thus it is not difficult to believe that Arata and his colleagues may have been pumping the hydrided or deuterided Pd lattice close to one of its resonances, as indeed Letts and Hagelstein reported when they described three one-phonon resonances at 8, 15, and 20 THz in their

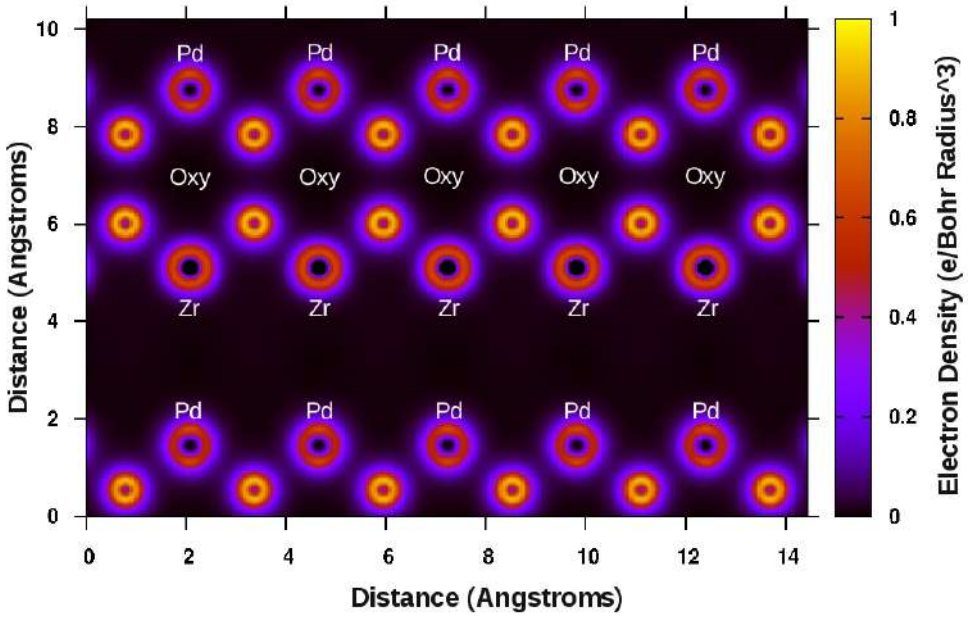

Figure 16. False color cross-sectional image of total charge density in a plane defined by the [110] and Z axes and intersecting the ZrO_2:Pd supercell. The aspect ratio of this figure is higher than 1:1 because the length of the [110] face diagonal is $\sqrt{2}$ times larger than the length of the unit cell in the X, Y, or Z dimensions.

two-laser paper [2]. What is also interesting is that Arata reports very little LENR activity when bulk Pd or powdered Pd was stimulated with the beam from the laser. Only when the Pd was in surface contact with a complex oxide did he observe high LENR activity and significant ^{4}He production.

8. DFT Study of the ZrO_2:Pd Interface

DFT studies of the ZrO_2:Pd interface were performed using a $2 \times 2 \times 2$ supercell in a manner similar to that described in Section 6 for the purpose of studying ferromagnetic activity and identifying which atomic species are most active. Figure 15 shows a false color image of the total charge density of the ZrO_2:Pd supercell sampled on a plane parallel to the YZ ([100]) plane and similar to those shown in Figs. 7, 9, and 11. The supercell lattice constant was set at 10.2164 Å, corresponding to a lattice constant of 5.1082 Å for each individual unit cell.

This view shows that the Pd and Zr atoms occupy the usual sites in the FCC supercell structure. However, the oxygen atoms are not visible in this view. In order to provide a view showing all 3 atomic species, we need to orient the horizontal axis in the crystallographic [110] direction instead of purely parallel to the Y-axis. Such a view is shown in Fig. 16.

As with the CaO:Pd and MgO:Pd structures, we generated spin-polarized images for the ZrO_2:Pd supercell. Figure 17 shows the spin-polarized image corresponding to the total charge image of Fig. 15, and Fig. 18 shows the spin-polarized image corresponding to the total charge image of Fig. 16. There are a number of striking features visible in Figs. 17 and 18. First, we note that the two rows of Pd atoms are no longer equally polarized; the Pd atoms located closest to the oxygen atoms are polarized about 20 times more strongly than the Pd atoms located closest to the Zr atoms. Likewise, the two rows of oxygen atoms shown in the figure are also no longer equivalent; the oxygen atoms

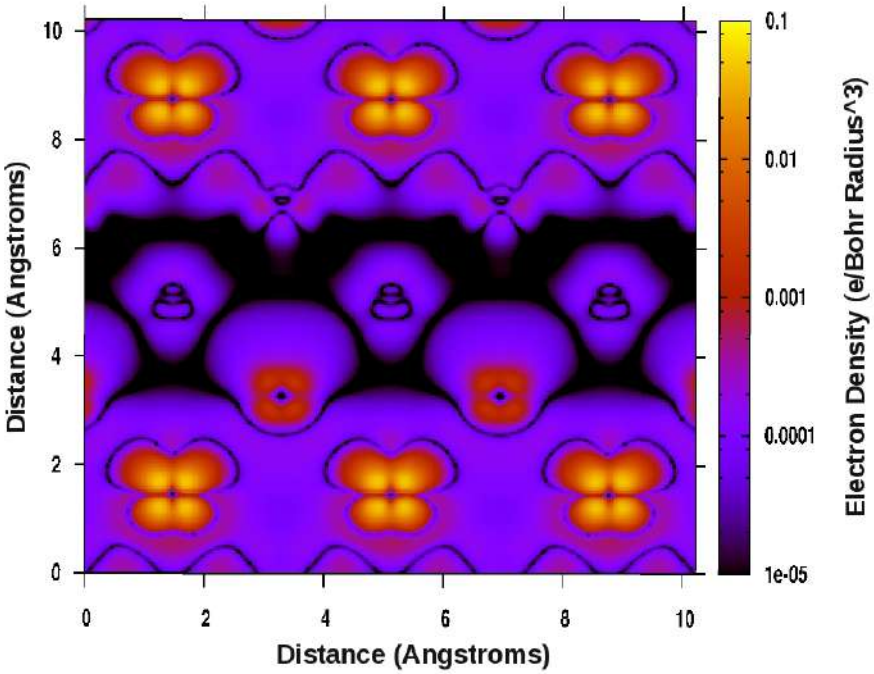

Figure 17. False color cross-sectional image of spin-up minus spin-down charge density taken parallel to the *YZ* plane (along the [100] crystal plane) and intersecting the ZrO_2:Pd supercell. The brightest features identify the lowest row of three Pd atoms, while the upper row of two Pd atoms (shown in red) is not as strongly magnetized. The magnetically inactive zirconium atoms are shown largely in violet and black with just a trace of red.

located closest to the Pd are much more strongly polarized than the ones near the Zr atoms. We also note that the Zr atoms themselves are very weakly polarized. This latter observation should not be especially surprising, because the lattice constant for the individual unit cells in this run was set to 5.1082 Å, corresponding to the minimum in the ZrO_2 energy curve. This is considerably less than the computed threshold of about 7 Å for the onset of spin polarization of the Zr atoms. Finally, both figures reveal exactly two zero crossings in traveling between any two Pd atoms and between any Pd and one of the neighboring strongly polarized oxygen atoms. Thus all of the Pd are ferromagnetically ordered, and furthermore, the oxygens are ferromagnetically polarized with respect to the Pd atoms, a situation very different from what is shown in Fig. 10, where the single hydrogen electron spin is polarized antiferromagnetically with respect to the Pd. One dimensional cross sections were also performed for the same ZrO_2:Pd supercell run whose two dimensional spin polarization false color images are shown in Figs. 17 and 18. In order to avoid undue increases in the length of the paper, their plots are presented in the on-line Supplemental Section.

The three structures discussed in this work may also be compared by providing their respective total supercell magnetic polarizations. For the MgO:Pd structure, the total magnetization is obviously zero, because there were no species whose interatomic separation was pushed beyond the threshold for spontaneous magnetization. For the CaO:Pd supercell, the total absolute magnetization was 5.57 Bohr magnetons, while for the ZrO_2:Pd supercell, the value was 8.61 Bohr magnetons. In both of the latter structures, the only atoms to become polarized are the Pd and the oxygens. The CaO:Pd supercell contains a total of 32 Pd and oxygen atoms, while the ZrO_2:Pd supercell contains a total of 48. Thus the ratio of polarized atoms between the two structures is $48/32 = 1.50$. As it turns out, the ratio of the

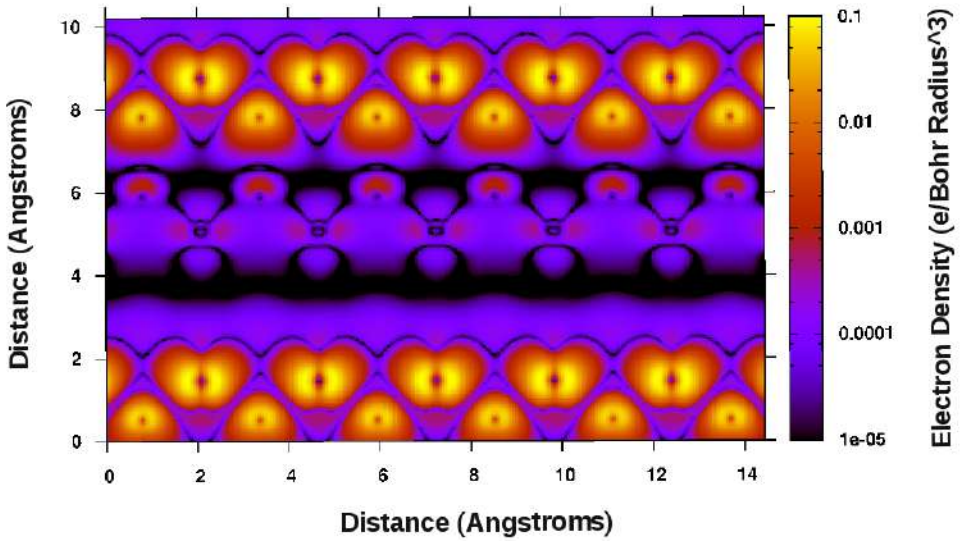

Figure 18. False color cross-sectional image of spin-up minus spin-down charge density in a plane defined by the [110] and Z axes and intersecting the ZrO_2:Pd supercell. The bright heart-shaped features identify the highly magnetized rows of Pd atoms, while the smaller bright features are the rows of oxygen atoms located near the highly magnetized Pd atoms. The less highly magnetized oxygen atoms are shown in red below their more highly magnetized counterparts. Once again, the magnetically inactive zirconium atoms are shown largely in violet and black. Finally, the less highly magnetized Pd atoms are not visible in this cross-sectional view.

two magnetizations was $8.61/5.57 = 1.54$. It is thus tempting to attribute the magnetization difference simply to the difference in the number of polarized atoms. However, the local variations in spin polarization shown in the figures suggest that this is an oversimplified picture, because all of the Pd and oxygen atoms in the CaO:Pd supercell are strongly polarized, while this is clearly not true for either the Pd or the oxygen atoms in the ZrO_2:Pd supercell. A more accurate picture can be obtained by making one dimensional plots of spin polarization through each of the two supercells and plotting the results on a linear scale instead of the logarithmic scale used in the false color images. Such a plot is shown in Fig. 19.

Care must be exercised in running one dimensional cross sections through the atoms, however, because the lattice symmetry induces nodes in the spin polarization along certain directions. In order to avoid sampling the spin polarizations along nodal lines, it was necessary to section the CaO:Pd supercell in the [001] direction (Z-direction) along a vector passing through the origin of coordinates. Thus the red line in the plot passes through Pd atoms at the 0.2 and 1.2 values of the Z-coordinate. The pair of minor peaks near 1.0 on the X-axis correspond to one of the oxygen atoms. For the ZrO_2:Pd supercell, it was necessary to perform our section in the [110] direction at an altitude of $Z = 0$ in order to pass through the antinodes in the spin polarization for the Pd atoms, and each pair of tall, green peaks represents one Pd atom. Even after exercising care to ensure our sections pass through the antinodes of the atomic polarization patterns, it is clear that the peak spin polarization is about two times larger for the ZrO_2:Pd structure than it is for the CaO:Pd. This is most probably attributable to the fact that the larger ZrO_2:Pd lattice constant pushes the Pd further up the magnetization curve than the CaO:Pd structure does.

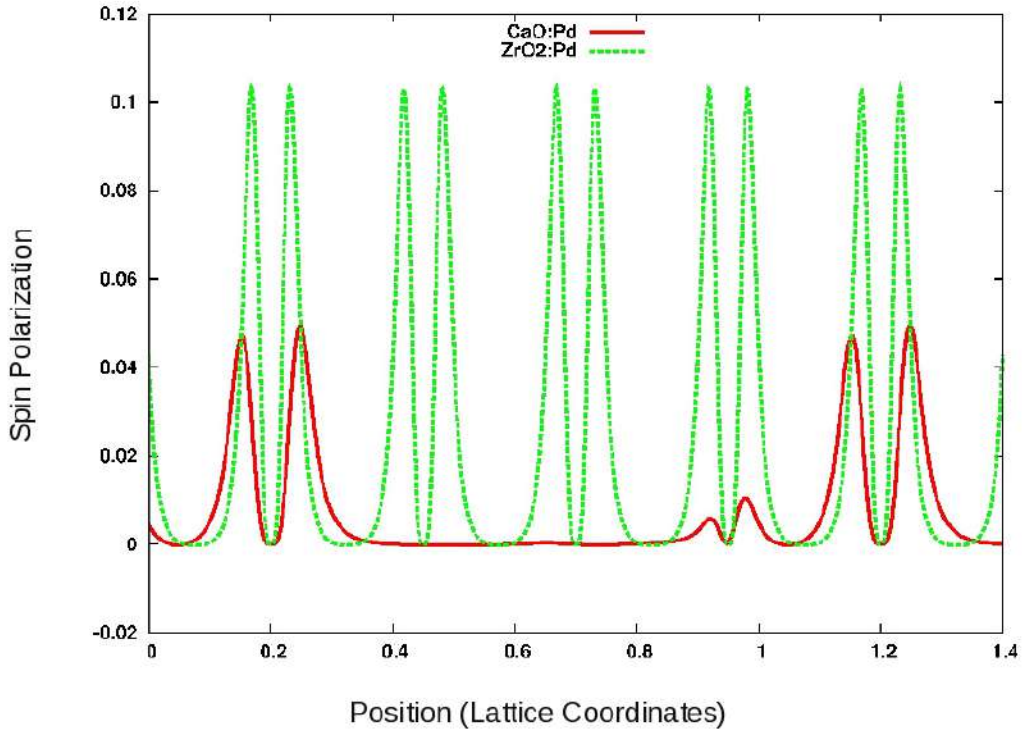

Figure 19. Plots of spin polarization (in units of electronic charges per cubic Bohr radius) versus position in the CaO:Pd supercell (red solid line) and in the ZrO_2:Pd supercell (green dotted line). The horizontal coordinates for the ZrO_2:Pd plot were divided by $\sqrt{2}$ to permit display on the same axis scale. The tall peaks in each of the plots represent the Pd atoms.

9. Summary

In summary, spin-polarized DFT computations have been useful in providing insight into the magnetic behavior of many of the transition metals on the Periodic Table in their elemental lattices. Most of the transition metals and a number of sp elements (including diamond, aluminum, silicon, germanium, selenium, tellurium, lead, and polonium) are predicted to exhibit ferromagnetic ordering when their lattices are placed in sufficiently high tensile stress. At the threshold lattice constant for the onset of this ferromagnetic ordering, we predict that the energy surface for the elemental lattice bifurcates into two stable solutions, one paramagnetic with a higher energy and one ferromagnetic with a lower energy. The paramagnetic sheet for the energy surface above threshold joins smoothly with the paramagnetic sheet below threshold, however the ferromagnetic sheet joins with the paramagnetic sheet in such a way that the energy is continuous, but its derivatives may exhibit jump discontinuities at the threshold. Most of the elements exhibit magnetization curves that rise very rapidly with lattice constant above threshold and then saturate at higher values, approaching well-defined asymptotes as the lattice constant grows. In most cases, the normalized values of these asymptotic magnetizations lie close to 1.0 Bohr Magneton per unpaired p or d electron spin, which is the expected limiting case for isolated atoms. Interestingly, we find that (with the possible exceptions of the Lanthanide and Actinide series) the atoms whose outermost electron shells contain only s electrons do not exhibit ferromagnetic ordering at any

practical value of lattice constant. This specifically includes all the Columns I and II elements and several elements on the right-hand edge of the Transition Metal Group such as zinc, cadmium, silver, and gold.

The results summarized above may now be applied to a variety of multilayer structures whose LENR results have been published during the past 15 years. The Mitsubishi Heavy Industries (MHI) team under Yasuhiro Iwamura reported successful observation of several different types of nuclear transmutations when using a structure consisting of alternating layers of CaO and Pd, both of which crystallize in the face-centered cubic (FCC) structure. The CaO unit cell lattice constant is about 4.815 Å, placing it above the threshold for the onset of spontaneous ferromagnetic ordering of Pd (4.50 Å when tensile stress is applied in all three dimensions, 4.69 Å when stress is applied in only two dimensions). By contrast, they reported negative experimental results when MgO was substituted for the CaO. The lattice constant for MgO is only 4.211 Å, placing it well below the thresholds for magnetization in Pd. Similarly, the Osaka University team under Yoshiaki Arata reported high LENR rates and ^{4}He production rates when their Pd nanoparticles were grown in intimate contact with ZrO_2, which also has an FCC lattice and a lattice constant of about 5.07 Å. They reported much lower LENR rates when bulk Pd or even finely divided Pd powder was used in the same experimental apparatus.

The search to identify the experimental parameters that most directly control LENR phenomena has posed and continues to pose difficult challenges for the community. The effect of magnetic fields upon measured LENR rates has been known for some time but is not yet well understood. Our results suggest the possible existence of an underlying order involving spontaneous magnetization that may tie together the work of several different teams and materials systems. It is hoped that these results will provide a number of mechanistic clues for the theoretical community as well as guidance for LENR materials specialists seeking to optimize reactor structures for various LENR applications of the future.

Acknowledgements

The DFT studies documented in this work are a direct outgrowth of US Navy research that was funded under the In-house Laboratory Independent Research (ILIR) Program, and we wish to gratefully acknowledge the strong support of Jeff Solka (the ILIR sponsor) and the Department Q management over the past 5 years. In addition, we wish to thank a number of dear colleagues for their inspiration, including Peter Hagelstein of the MIT Electronics Research Laboratory, the LENR teams at the NASA Langley and Glenn facilities, and especially Olga Dmitriyeva and Rick Cantwell of Coolescence, who were instrumental in suggesting the potential value of spin-polarized calculations in elemental metal systems.

References

[1] J.O.M. Bockris, R. Sundaresan, Z, Minevski and D. Letts, Triggering of heat and sub-surface changes in Pd–D systems, *ICCF Conference Proceedings*, Vol. 4, 1993.

[2] D. Letts and P.L. Hagelstein, Stimulation of optical phonons in deuterated palladium, *ICCF Conference Proceedings*, Vol. 14, 2008.

[3] Y. Iwamura, T. Itoh, M. Sakano, N. Yamazaki, S. Kuribayashi, Y. Terada, T. Ishikawa and J. Kasagi, Observation of nuclear transmutation reactions induced by D_2 gas permeation through Pd complexes, *ICCF Conference Proceedings*, Vol. 11, 2004.

[4] Y. Arata and Y.C. Zhang, Development of compact nuclear fusion reactor using solid pycnodeuterium as nuclear fuel, *ICCF Conference Proceedings,* Vol. 10, 2002.

[5] P. Hohenberg and W. Kohn, Inhomogeneous electron gas, *Phys. Rev.* **136** (1964) B864–B871.

[6] W. Kohn and L.J. Sham, Self-consistent equations including exchange and correlation effects, *Phys. Rev*. 140 (1965) A1133–A1138.

[7] P. Giannozzi, S. Baroni, N. Bonini, M. Calandra, R. Car, C. Cavazzoni, D. Ceresoli, G.L. Chiarotti, M. Cococcioni, I. Dabo,, A. Dal Corso, S. de Gironcoli, S. Fabris, G. Fratesi, R. Gebauer, U. Gerstmann, C. Gougoussis, A. Kokalj, M. Lazzeri, L. Martin-

Samos, N. Marzari, F. Mauri, R. Mazzarello, S. Paolini, A. Pasquarello, L. Paulatto, C. Sbraccia, S. Scandolo, G. Sclauzero, A.P. Seitsonen, A. Smogunov, P. Umari and R.M. Wentzcovitch, *J. Phys.: Condensed Matter* **21** (2009) 395502.

[8] R.W.G. Wyckoff, *Crystal Structures*, Wiley, New York, 1963.

[9] T. Hioki, N. Takahashi, S. Kosaka, T. Nishi, H. Azuma, S. Hibi, Y. Higuchi, A. Murase and T. Motohiro, Inductively coupled plasma mass spectrometry study on the increase in the amount of Pr atoms for Cs–Ion–implanted Pd/CaO multilayer complex with deuterium permeation, *Jap. J. Appl. Phys.* **52** (2013) 107301-1–107301-8.

[10] Y. Arata and Y.C. Zhang, Development of compact nuclear fusion reactor using solid pycnodeuterium as nuclear fuel, *ICCF Conference Proceedings*, Vol. 10, 2003.

[11] See, for example, Y. Arata, N. Abe and T. Oda, Fundamental phenomena in high power CO_2 laser welding (Report I): atmospheric laser welding (welding physics, process & instrument), *Trans. JWRI* **14**(1) (1985) 5–11.

Appendix A

Appendix B

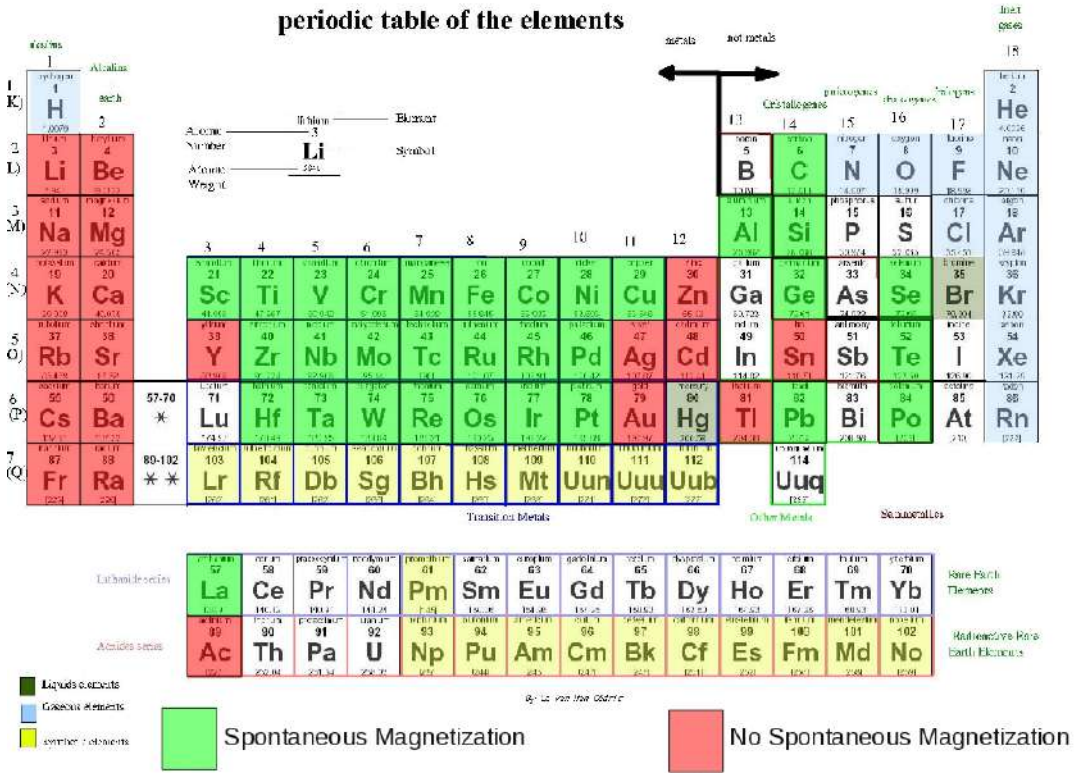

Figure 20. Appendix B: Periodic Table of the elements.

Supplementary Figures

Table 1. Appendix A: Table of computed and accepted values of lattice constant

Element	Lattice type	Pseudopotential file name	Computed a	Accepted a	% Error
Actinium	Face-Centered Cubic	Ac.pbe-mt-fhi.UPF	5.3199	5.31	0.186
Aluminum	Face-Centered Cubic	Al.pbe-rrkj.UPF	4.0219	4.0495	–0.682
Antimony	Hexagonal Close Packed	Sb.pbe-rrkj.UPF	3.4163	3.33	2.592
Barium	Body-Centered Cubic	Ba.pbe-nsp-van.UPF	4.982	5.02	–0.757
Beryllium	Hexagonal Close Packed	Be-pbe-rrkjus.UPF	2.3035	2.2858	0.774
Cadmium	Hexagonal Close Packed	Cd.pbe-n-van.UPF	3.117	2.9794	4.618
Calcium	Face-Centered Cubic	Ca-pbe-nsp-van.UPF	5.5458	5.5884	–0.762
Carbon (Diamond)	Face-Centered Cubic	C.pbe-rrkjus.UPF	3.5685	3.57	–0.042
Cesium	Body-Centered Cubic	Cs-pbe-mt-fhi.UPF	5.8912	6.141	–4.068
Chromium	Body-Centered Cubic	Cr.pbe-sp-van.UPF	2.8552	2.91	–1.883
Cobalt	Hexagonal Close Packed	Co-pbe-nd-rrkjus.UPF	2.5184	2.5071	0.451
Copper	Face-Centered Cubic	Cu.pbe-d-rrkjus.UPF	3.6315	3.61	0.596
Germanium	Face-Centered Cubic	Ge.pbe-mt_fhi.UPF	5.8722	5.6575	3.795
Gold	Face-Centered Cubic	Au.pz-nd-rrkjus.UPF	4.0204	4.08	–1.461
Hafnium	Hexagonal Close Packed	Hf-pbe-mt-fhi.UPF	3.2194	3.1964	0.720
Iridium	Face-Centered Cubic	Ir-pbe-n-rrkjus.UPF	3.839	3.9092	–1.796
Iron	Body-Centered Cubic	Fe-pbe-nd-rrkjus.UPF	2.8783	2.87	0.289
Lanthanum	Hexagonal Close Packed	La-pbe-nsp-van.UPF	3.662	3.75	–2.347
Lead	Face-Centered Cubic	Pb-pbe-d-van.UPF	5.007	4.9508	1.135
Lithium	Body-Centered Cubic	Li-pbe-n-van.UPF	3.5092	3.51	–0.023
Magnesium	Hexagonal Close Packed	Mg-pz-n-vbc.UPF	3.1598	3.21	–1.564
Manganese	Body-Centered Cubic	Mn.pbe-sp-van.UPF	2.8649	2.85	0.523
Molybdenum	Body-Centered Cubic	Mo-pbe-mt-fhi.UPF	3.2148	3.147	2.154
Nickel	Face-Centered Cubic	Ni.pbe-nd-rrkjus.UPF	3.52	3.524	–0.114
Niobium	Body-Centered Cubic	Nb-pbe-nsp-van.UPF	3.3051	3.3	0.155
Osmium	Hexagonal Close Packed	Os.pbe-mt-fhi.UPF	2.8072	2.7344	2.662
Palladium	Face-Centered Cubic	Pd-pbe-rrkjus-4d10.UPF	3.974	3.8907	2.141
Platinum	Face-Centered Cubic	Pt-pbe-nd-rrkjus.UPF	3.9854	3.92	1.668
Polonium	Simple Cubic	Po-pbe-mt-fhi.UPF	3.2074	3.359	–4.513
Potassium	Body-Centered Cubic	K-pz-n-vbc.UPF	5.2401	5.23	–0.194
Rhenium	Hexagonal Close Packed	Re.pbe-mt-fhi.UPF	2.8139	2.761	1.916
Rhodium	Face-Centered Cubic	Rh-pbe-rrkjus.UPF	3.959	3.8	4.184
Rubidium	Body-Centered Cubic	Rb-pbe-mt-fhi.UPF	5.468	5.585	–2.095
Ruthenium	Hexagonal Close Packed	Ru.pbe-n-van.UPF	2.779	2.7059	2.702
Scandium	Hexagonal Close Packed	Sc.pbe-nsp-van.UPF	3.303	3.309	–0.181
Selenium	Hexagonal	Se.pbe-van.UPF	4.4695	4.36	2.511
Silicon	Face-Centered Cubic	Si.pbe-rrkj.UPF	5.5085	5.4309	1.429
Silver	Face-Centered Cubic	Ag-pbe-d-rrkjus.UPF	4.1333	4.09	1.058
Sodium	Body-Centered Cubic	Na-pbe-sp-van-ak.UPF	4.1283	4.2906	–3.783
Strontium	Face-Centered Cubic	Sr-pbe-sp-van.UPF	6.0934	6.08	0.220
Tantalum	Body-Centered Cubic	Ta-pbe-nsp-van.UPF	3.3418	3.3013	1.227
Technetium	Hexagonal Close Packed	Tc.pbe-mt-fhi.UPF	2.776	2.735	1.499
Tellurium	Hexagonal	Te.pbe-rrkj.UPF	4.5050	4.45	1.236
Thallium	Hexagonal Close Packed	Tl-pbe-mt-fhi.UPF	3.3538	3.4566	–2.974
Tin	Tetragonal	Sn-pbe-d-rrkjus.UPF	5.9175	5.8318	1.470
Titanium	Hexagonal Close Packed	Ti-pbe-sp-van.UPF	2.923	2.9508	–0.942
Tungsten	Body-Centered Cubic	W-pbe-nsp-van.UPF	3.1951	3.1652	0.945
Vanadium	Body-Centered Cubic	V-pbe-n-van.UPF	3.0078	3.02	–0.404
Yttrium	Hexagonal Close Packed	Y-pbe-nsp-van.UPF	3.6318	3.65	–0.499
Zinc	Hexagonal Close Packed	Zn-pbe-van.UPF	2.7353	2.6649	2.642
Zirconium	Hexagonal Close Packed	Zr-pbe-nsp-van.UPF	3.2254	3.232	–0.204

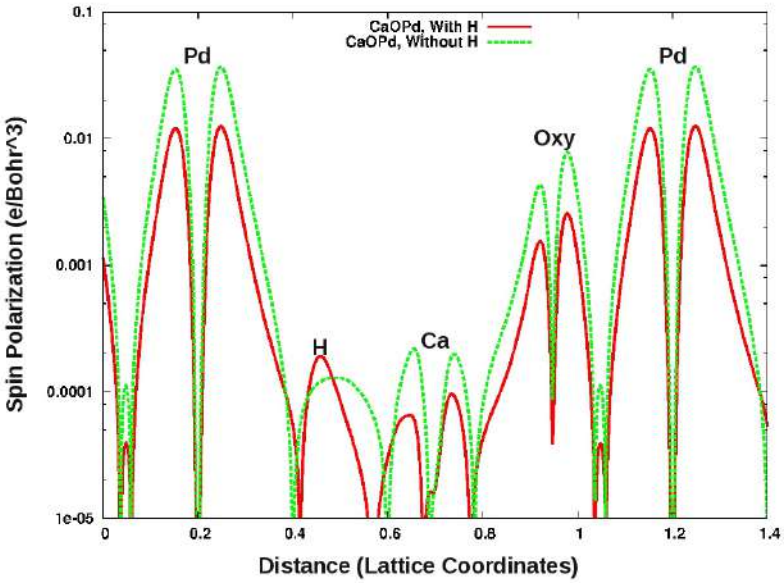

Figure 21. Supplementary Figure S1.

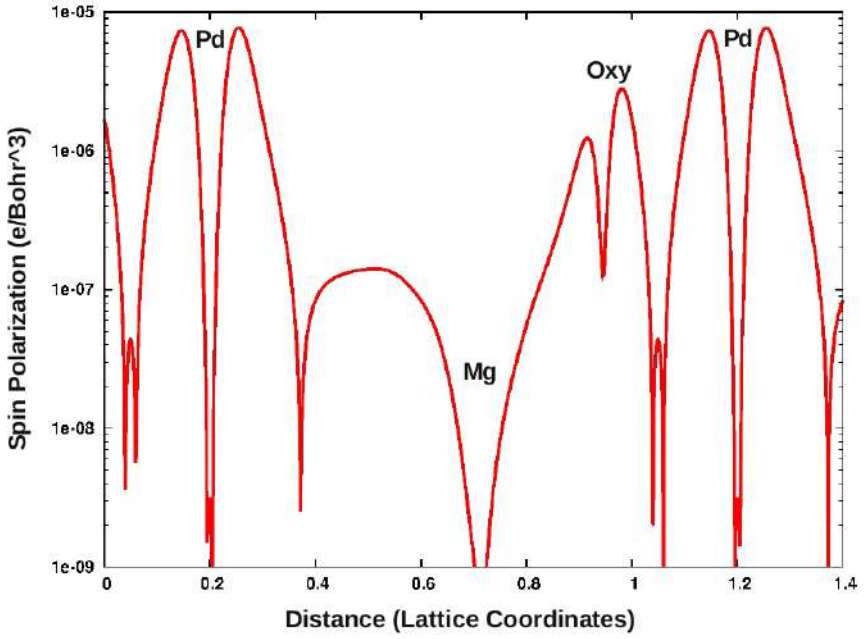

Figure 22. Supplementary Figure S2.

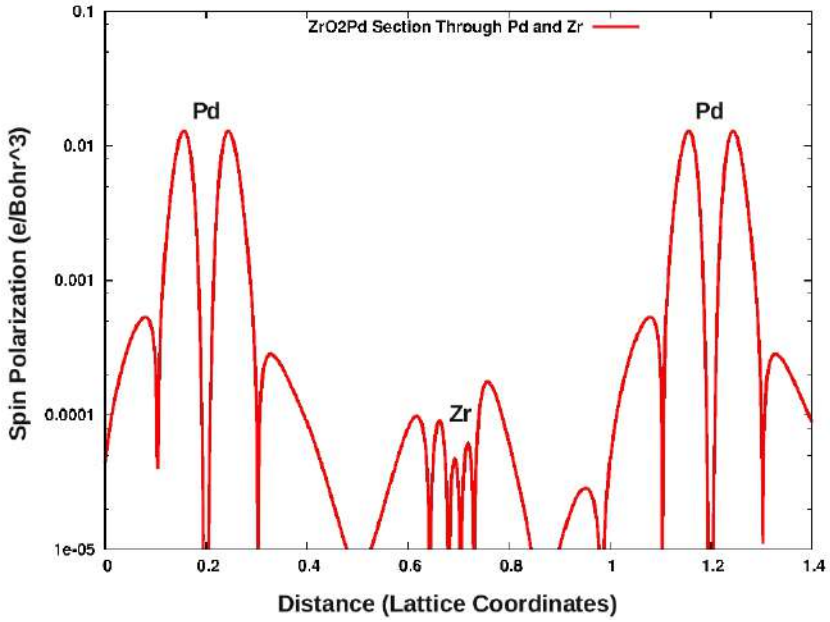

Figure 23. Supplementary Figure S3.

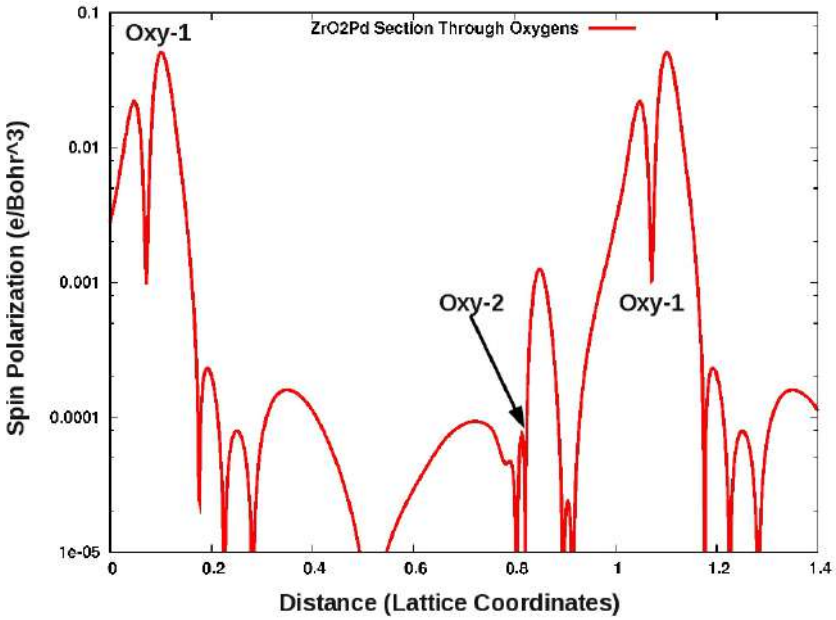

Figure 24. Supplementary Figure S4.